EXPECTED HOST GALAXY PROPERTIES OF PTA DETECTABLE MASSIVE BLACK HOLE BINARIES

By

Katharine Cella

Under the advisement of Dr. Stephen Taylor

Submitted December 6, 2021 in partial fulfillment of the requirements for the degree of Honors Bachelor of Arts in Physics at Vanderbilt University

ABSTRACT

Massive black hole binaries (MBHB) produce gravitational waves (GW) that will be detectable with pulsar timing arrays within the next few years. We determine the properties of the host galaxies of MBHB at the time they are producing detectable GW. The population of MBHB systems we evaluate is from the Illustris cosmological simulations taken in tandem with post processing semi-analytic models of environmental factors in the evolution of binaries. Upon evolving to the frequency regime detectable by pulsar timing arrays, we calculate the detection probability of each system using a variety of different values for red and white noise. We average over multiple realizations of the universe by re-sampling the host galaxy properties using a kernel density estimator to approximate the statistical distributions of the universe. Excitingly, we find that detectable systems have host galaxies that are clearly distinct from the overall population. With conservative noise factors, we found that stellar metallicity, for example, peaks at approximately twice solar metallicity as opposed to the total population of galaxies which peaks at approximately solar metallicity. Additionally, the most detectable systems are brighter and more red in color than the overall population. These results can be used to develop effective search strategies for identifying host galaxies and electromagnetic counterparts following GW detections.

ACKNOWLEDGMENTS

I extend my gratitude to my thesis advisor, Professor Stephen Taylor, for his consistent guidance in my almost two years of work on this project. Thank you for all your wisdom in understanding astrophysics and in preparing for my future beyond college. A special thank you to Dr. Luke Kelley for his help in providing data and teaching me about GW astrophysics. Thank you to the members of thesis committee: Professor Scherrer, Professor Holley-Bockelmann, and Professor Varga for taking time to consider my thesis. Finally, thank you to the Department of Physics and Astronomy for providing the opportunity to write this thesis.

TABLE OF CONTENTS

LIST OF FIGURES

CHAPTER 1

Introduction and Background

Gravitational waves (GW) were first predicted by Albert Einstein in 1916 as an output of his general theory of relativity to be ripples in space-time caused by highly massive objects. However, these perturbation in space-time are so small that until very recently they were no direct detections of them (there have been indirect detections like the one described in Hulse & Taylor (1975)). In 2015, the news was filled with the discovery from the LIGO detector, which made the first detection of GW, a remarkable confirmation of a 99 year old prediction (Abbott et al., 2016). The detected GW are in a higher frequency regime characteristic of colliding neutron stars. At lower frequencies, on the order of nanohertz, the detectable GW are produced by massive black hole binaries (MBHB).

Massive black holes (MBH) are found at the center of large galaxies. Galaxies are known to grow hierarchically–by merging with other galaxies (McWilliams et al., 2014). As large galaxies merge, the black holes (BH) at their centers merge as well. This leads to the formation of MBHB, as when two MBH merge, they become gravitationally bound. Over many gigayears the MBHB go through a process called hardening where they lose energy and decrease in separation. The black holes are thought to harden by a variety of environmental factors, namely stellar scattering, dynamical friction, and interactions with the gaseous disk. A more detailed description of these factors may be found in Sec. 2.2, but a brief overview is given here. Dynamical friction is the transfer of energy from moving black holes to the more slowly moving background matter of stars, gas, and dark matter in a galaxy (Antonini & Merritt, 2011; Merritt & Milosavljević, 2005). Separation also decreases by the system losing energy by "sling-shotting" background stars away (Merritt, 2013). If the density of the gas accreting onto the MBH is high enough, a circumbinary disk is able to form, and the viscous drag caused by the black holes moving through this circumbinary disk can drive the hardening of the binary system into the separation regime where GW dominates (Gould & Rix, 2000). When the binary systems has hardened enough and the galaxies have a small enough separation, the system begins to evolve primarily to the lose in energy due to the emission of GW. At this point the inspiralling MBHB is producing continuous-wave GW, the earlier stages of which can be observed by PTA. Often it becomes decoupled from its environment at separations below $\sim$1pc (Burke-Spolaor et al., 2019) and thus its evolution is only dependent on GW.

These very small distortions of space-time caused by these rotating massive black holes (MBH) are not detectable with any earthly instrument. However, it is possible using an array of natural detectors scattered throughout our galaxy. These objects are pulsars, specifically millisecond pulsars, that rotate with millisecond periods. Millisecond pulsars produce a stream of light that, as it rotates, hits Earth at extremely regular

intervals, so regular, in fact, that they are one of the most reliable timers that exist. This reliability can be leveraged to detect the slight perturbation in space-time resulting from GW. They are detected in the form of timing delays of the time of arrival (TOA) on the light pulse from the pulsars (Burke-Spolaor et al., 2019). The GW affect both the space-time at each pulsar and at Earth but at different times. Pulsar timing can detect a GW passing either of these locations in the "pulsar term" or the "earth term" and is seeking correlation between the variance in these two terms indicating a GW detection. However, for a confidant detection of GW we need correlation between these two terms in many pulsars.

The sources of GW are hundreds of megaparsecs away and thus can be treated as a plane wave (Rosado et al., 2015). The effect of the GW on the TOA can be understood as a Doppler-shift of the pulse frequency meaning the observed redshift will varies with time. At time t,

$$z(t) = \frac{\hat{p}^i \hat{p}^j}{2(1+\hat{\Omega}\cdot\hat{p})}[h_{ij}(t) - h_{ij}(t-t_l)] \tag{1.1}$$

where h_{ij} is the strain, or space-time perturbation. The parameter $\hat{p}$ is a vector pointing to the pulsar position, $\hat{\Omega}$ is the vector in the direction that the GW propagates, and l is the distance between the pulsar and the solar system barycenter. The perturbation to TOA is the integration of the redshift over time (Anholm et al., 2009).

Upon considering multiple pulsars the relative positions of the pulsars becomes relevant in determining their correlation. This gives rise to an important and commonly shown curve, the "Hellings and Downs" curve (Hellings & Downs, 1983), that shows how the correlations appear as a function of the angle between pulsars. This is the distinctive fingerprint of the GW background signal in PTA data.

There are 3 PTA in use: the European (EPTA, Kramer & Champion (2013)), NANOGrav (McLaughlin, 2013), and Parkes (PPTA, Manchester et al. (2013)). The International Pulsar Timing Array (IPTA, (Hobbs et al., 2010) is the combination of the data from the former three. There are two different types are GW signals that these PTAs could detect in the near future. The most likely to be detected first is the GW background (GWB), a superposition of the GW signals of many systems (Kelley et al., 2018), but individually resolvable sources, or single sources, while perhaps not the first signal to be detected, can be detected above the background if they are close enough or massive enough. Being close or massive increases one of the primary parameters in the strain of binary:

$$h(f_{K,r}) = \sqrt{\frac{32}{5}}\frac{(G\mathscr{M})^{5/3}}{c^4 D}(2\pi f_{K,r})^{2/3}. \tag{1.2}$$

We see Equation 1.2 contains the mass in the parameter $\mathscr{M}$, the chirp mass, which relates the individual black hole masses m_1 and m_2 by $\mathscr{M} = [m_1 m_2]^{3/5}/[m_1+m_2]^{1/5}$. It contains distance in D, the comoving distance. These parameters are the most important physical factors in the magnitude of the strain. This magnitude is what allows an individual source to be distinguished from the background and the noise of the PTA. There

are multiple ways to quantitatively describe a systems ability to be detected–its signal to noise ratio (SNR), its detection probability (DP), or its time to detection, for example.

There are other papers that have done work in this area. Kelley et al. (2018) uses data from the Illustris simulation to predict the detection prospects and properties of MBHB single sources. They find that single sources are likely to be detected and their detection prospects have a weak dependence on properties such as eccentricity and environmental coupling. However, the noise properties, particularly the red noise, have a larger affect, changing the time of detection from $\sim 10-15$ yr, if there is no red noise, to $\sim 20-30$ yr with a large red noise model. The GWB is even more greatly affected in detection time by variation in red noise. Kelley et al. (2018) quantified detection prospects by time of detection, but there are different way to quantify detection prospects. Rosado et al. (2015) calculates the detection probability as a metric for how detectable a system is, and similarly finds that the GWB is more likely to be detected before a single source, but the detection probability of detecting a single source is not negligible. DeGraf et al. (2021) use the Illustris simulation to probe the morphologies of the mergers that indicate MBHB and found morphological evidence of recent mergers in PTA detectable systems, but the timescale is such that electromagnetic follow up may not be able to detect this. Additionally, they find the mergers occur along the $M_{\rm BH}-M_{\odot}$ and show how this affects the star formation rate of the galaxy.

If there is a detection of a GW single source from the analysis of the data from PTA, it is then of great importance to determine the source galaxy. Connecting GW information with its electromagnetic counterpart by identifying the GW source allows insight into the types of galaxies producing GW, the dynamics of black hole binary interactions, both with each other as well as the surrounding environment, and potentially even tests of gravity and insight into the nature of black holes (Burke-Spolaor et al., 2019). However, the spacial resolution of PTA are very poor. The sky-localization being on the order of hundreds of deg^2 (Sesana & Vecchio, 2010), it is unable to suggest more than an area of the sky that the detected single source originated from. Thus, if we could know the expected properties of the galaxies that produce detectable GW then we could rank the galaxies in the suggested area of the sky by their likelihood of being the host galaxy. This is the goal on our work: to determine the host-galaxy properties of the most detectable MBHB systems.

Cosmological hydrodynamical simulations are very useful to look at these properties. They contain information about the galaxy evolution and growth which is directly related to the hosted black hole evolution. We use the Illustris simulation (Vogelsberger et al., 2014a,b; Genel et al., 2014) and calculate and add on more detail of the MBHB evolution to forecast ahead to the time when systems would be PTA detectable. At the forecasted future time we collect the galaxy properties from the simulated host galaxies in Illustris and use them to quantify the properties of both the binary and the host galaxy at the time of detection with the future goal of connecting them with electromagnetic counterparts to achieve multi-messenger detection. We focus solely on the PTA regime where the simulation should have the correct coverage of BH masses.

This thesis is laid out as follows. In Chapter 2 we outline the details of how we chose and evolved the MBHB systems within Illustris into the PTA band, and then how the host galaxy characteristics were pulled from these systems and weighted appropriately to indicate which are the most detectable. In Chapter 3 we look at the distribution of these host galaxy properties which allow us to rank galaxies by their likelihood of being a single source host.

CHAPTER 2

Methods

In this chapter we detail the process of selecting and evolving MBHB systems in Illustris. We determine the time that a MBHB would be PTA detectable and access the host galaxy properties at this time. Each of these host galaxy properties is then weighted appropriately by its detectability.

2.1 Merging massive black holes within Illustris

In order to analyze the most likely host galaxies we used the Illustris cosmological simulations. Illustris simulates a cubic volume with a side length of 106.5 Mpc self consistently through 136 redshifts. At each of these redshifts is a snapshot of the properties of all the galaxies being evolved in the simulation. Though a very small portion of the whole universe, this is a large enough slice to be useful in determining the statistical properties of the large mass galaxies we are interested in. We use the highest resolution "Illustris-1" volume, which included around six billion gas cells and dark matter particles with mass resolutions of $1.3 \times 10^6\ M_\odot$ and $6.3 \times 10^6\ M_\odot$, and softening lengths of 710pc and 1400pc. At redshift zero, the simulation volume contains $\sim 6 \times 10^8$ stars and over 30,000 MBHs.

Over the course of the simulation, MBHs are seeded with an initial mass of $\sim 10^5 M_\odot$ into halos having a mass above $7 \times 10^{10} M_\odot$, and are then allowed to grow via accretion and mergers with other MBHs. In order to avoid artificial numerical scattering, MBH particle dynamics are not evolved self-consistently, and are instead re-positioned to the centers of their parent halo. When two black holes come within 710pc of one another, they are "merged" instantly. This is not physically representative of real MBHB, but Illustris does not use enough detail to go more in depth to the dynamics of the binary interactions. However, in our analysis, we consider this "merger" to be the point in time when a binary forms from the two MBHs. It is important to note that at this "merger" point in Illustris, the MBH are usually separated by $\sim$kpc, and thus are not yet gravitational bound as a true binary. We subsequently run the detailed binary evolution in post-processing using semi-analytic models (see Sec. 2.2). The black hole re-positioning occasionally leads to spurious mergers for MBHs near the seed mass, and thus we only include MBHs with $M > 10^6 M_\odot$ in our analysis (Blecha et al. 2016; see also the discussion in Katz et al. 2020).

2.2 Evolving massive black-hole binaries into PTA sensitivity band

Illustris merges the BH once they are within 710pc of each other and does not have the precision to include detail about the dynamics of BH mergers. In order to fill in the gaps in detail, we post-processed the Illustris MBH mergers with our own binary evolution scheme which includes both environmental factors and, eventually, gravitational waves. This post-processing begins when the MBHs are merged by Illustris, and persists

through until the binaries enter the PTA GW band. The evolution considers the three environmental factors described in Sec. 1—dynamical friction, stellar loss-cone scattering, and viscous drag within a circumbinary disk which allow the system to reach separations necessary to evolve due to the emission of GW (Holley-Bockelmann & Khan, 2015). The initial parameters for determining the evolution due to these affects are interpolated from the density and velocity profiles from each MBHB host galaxy. Our current analysis treats all binaries as circular, but eccentric binary evolution can also be included in future analysis.

A detailed explanation of dynamical friction can be found in Antonini & Merritt (2012), and the specifics of our implementation are found in Kelley et al. (2017). For stellar scattering, we only consider the case of two-body scattering and use the model of Magorrian & Tremaine (1999) with a central object amidst a isotropic and spherical background with a simple modification of the radius of interaction. For refilling, we use a logarithmic fraction $\mathscr{F}_{\rm refill}$ which includes the effects of the 'loss-cone'–or area of stars that interact with the binary–refilling. When considering viscous drag there are three regions of the disk of importance: 1) radiation & Thomson, 2) thermal & Thomson, and 3) thermal & free-free. Each is modeled with density profiles that come from the accretion rate in Illustris. More details of the disk prescription may be found in Kelley et al. (2017).

After evolving from the Illustris merger separation due to these environmental factors the binaries may reach a separation that is small enough that the hardening is dominated by the emission of GW. The hardening rate due to GW is found in (Peters, 1964):

$$\frac{da}{dt} = -\frac{64G^3}{5c^5}\frac{M_1 M_2 (M_1+M_2)}{a^3} \tag{2.1}$$

where a is the semi-major axis. Thus we integrate and,

$$t_{GW} = \frac{5c^5}{64G^3}\frac{a_0^4 - \mathscr{R}_{\rm crit}^4}{M_1 M_2 M} \tag{2.2}$$

$$\approx 10^{10}{\rm yr}\left(\frac{a_0}{0.01{\rm pc}}\right)^4 \times \left(\frac{M}{2x10^7 M_\odot}\right)^{-3} \times \left(\frac{2+\mu+1/\mu}{4}\right) \tag{2.3}$$

with total mass $M = M_1 + M_2$, mass ratio $\mu \equiv M_2/M_1$, initial step a_0 and critical separation $\mathscr{R}_{\rm crit}$. We assume the GW signal from binaries ends at the Inner-most Stable Circular Orbit (ISCO), where the binary 'coalesces'; so $R_{crit} = R_{isco}(J = 0.0) = 3R_s$. The most massive binaries can evolve from a parsec separation, but from $10^6 - 10^8 M_\odot$, the majority of systems, environmental factors are required in order to reach the necessary separations for GW emission to dominate. Once a binary reaches the GW regime that is detectable by the PTA we then acquire the properties of the host galaxy at this time in Illustris. While the details of the binary evolution are not included in Illustris, the host galaxy continues to evolve over this time scale required to harden and thus provides information regarding its properties when PTA detectable.

2.3 Tracking host galaxies over cosmic time within Illustris

In order to access the properties of a specific galaxy in the simulation one needs the subhalo ID and the snapshot number (in our case a subhalo in Illustris is treated the same as a galaxy). Having the subhalo ID and snapshot directly after the black holes "merges" in Illustris allows us to follow the merger tree file to the future scale factor of the subhalo when it would produce GW in the PTA sensitivity band. This gives the subhalo ID and snapshot of the galaxy in Illustris when our post-processing deems it is detectable.

The scale factor tells the time that the MBH system has evolved to produce GW that are PTA detectable, in other words, they have a period of 12 years (observed 24 year orbital period). The conversion between the scale factor, a, and redshift, z, is trivial, $z = (1-a)/a$, and the resulting redshift corresponds to a snapshot in Illustris. The first snapshot that's corresponding redshift is greater than this calculated redshift is the snapshot number at which to analyze the galaxy properties as it is the first snapshot after the system is PTA detectable.

Determining the new subhalo ID is not trivial as the subhalo ID is not unique to a certain subhalo through time, it is only unique in its snapshot. The same subhalo has different ID numbers in different snapshots. To find the right subhalo, we had to navigate the merger tree files. The sublink merger tree for the main descendant branch (sublink_mdb) includes arrays of all the snapshot number of the descendants of this system, carrying with each of them the ID number at that snapshot. However, if the system is not part of the main descendant branch, the file includes the data for all the subhalos in the tree except those that are the progenitors of the subhalo the file was accessed for. Figure 1 gives a visual depiction of this idea. If the system is not in the main descendant branch, then the descendants are in a depth-first ordering that starts at the smallest redshift and ends with the system for which the file belongs to. Since the file might contain multiple of the same snapshot number, special care must be taken to find the correct one. Because of the depth first ordering that ends on the system of interest, the last occurrence of the snapshot of interest must be the correct one. The index of the correct system in the array of snapshots is the index of the system's subhalo ID in the ID array. There were 4 systems where the merger tree files skipped over the snapshot where the desired system should have been. This is a work around in Illustris to deal with the issue that a smaller subhalo is passing through the larger one we care about. These are removed from the set of systems.

The Illustris API allows easy access to the host galaxy properties for each MBH systems using its subhalo ID and snapshot. The properties that this thesis will take a close look at are the redshift, galaxy mass, stellar metallicity, specific star formation rate, and color magnitude relationship. Additionally, we will look at the chirp mass and frequency of the binary to compare with the other properties of the host galaxy. In order to understand the properties of the host galaxies systems that are the most likely to be detected, the property histograms must be weighted by some metric to indicate their likelihood of being detected. We chose to use the DP (Rosado et al., 2015) to weight our system, but we compare the DP weighting to weighting by the strain, SNR, and simply a frequency cutoff for MBH systems.

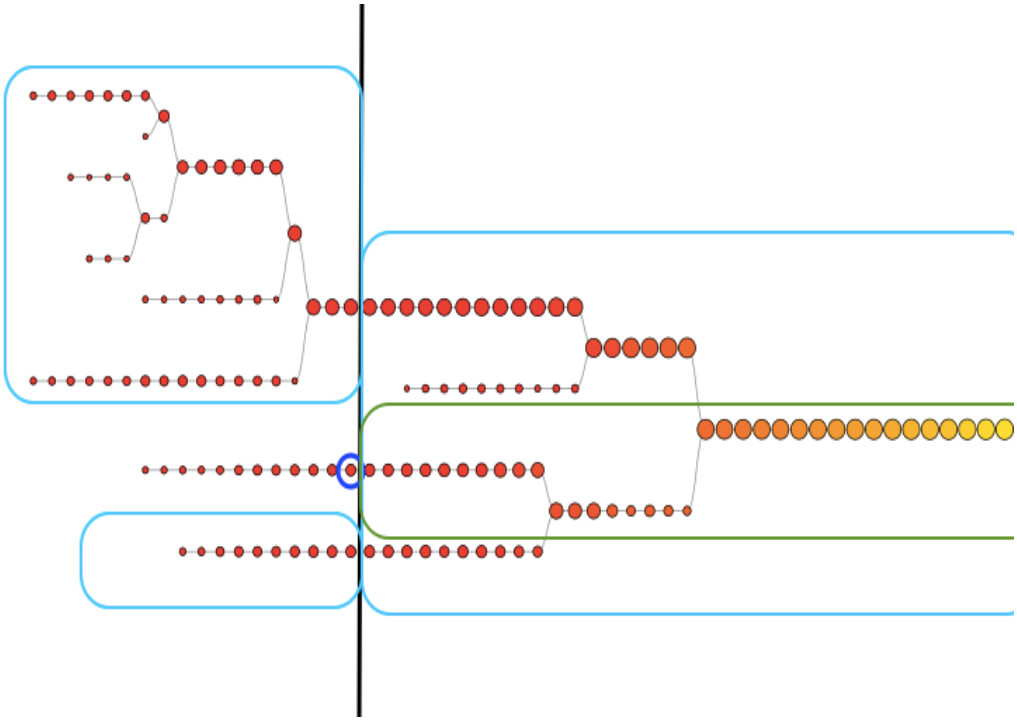

Figure 1: The dark blue circled system is the one for which we are retrieving the merger tree (referred to as "system of interest"). We are concerned with the information to the right of the black line (smaller redshift and later time). If the blue circled system is in the main descendant branch, then only the systems within the green box are included. If it is not in the main descendant branch, then all the systems within the blue boxes are included. In both cases the blue circled system is the last in the arrays.

2.4 Detection Probability and Pulsar Timing Array Model

With 3947 PTA detectable systems from Illustris above the mass cut and well behaved as described by Kelley et al. (2018), we re-sampled and created 1000 realizations of the universe. In each of these realizations we re-sampled $\sim$2.5 million systems using a kernel density estimator (KDE) over each time step of the 3947 systems that would produce GW in the PTA detectable frequency range. Shrinking the population to just in the PTA detectable frequency band before re-sampling makes the process more computationally tractable, and these are the only systems we care about to begin with. We determine this total number of systems to draw by associating each system that will become PTA detectable at each of its time steps with the result of a Poisson process $P(\Lambda_{ij})$, with Λ_{ij} being,

$$\Lambda_{ij} = \frac{1}{V_{ill}} \frac{dV_c(z_{ij})}{dz_{ij}} \Delta z_{ij}, \tag{2.4}$$

where the comoving volume element is,

$$dV_c(z) = 4\pi(1+z)^2 \frac{c}{H(z)} d_c^2(z) dz. \tag{2.5}$$

$H(z)$ is the Hubble constant at redshift z, with corresponding comoving distance d_c, Δz_{ij} is the redshift step-size for this binary and time step. The 2.5 million systems is the sum of the Poisson factors of the systems in a detectable frequency range and thus is the number that we draw. Instead of creating different realizations by drawing different Poisson values for each system as is done in Kelley et al. (2018), we choose a different and more computationally intensive strategy of drawing new samples for each realization. We did this to avoid finiteness issues. We have the host galaxy properties of 3947 systems, and they repeat for each time step. The time span where the binary is producing PTA detectable GW is not long enough to necessitate acquiring the properties at different Illustris snapshots. Thus there are many repeats of the same properties. In order to avoid the DP weighted plots being dominated by repeats of the same exact system in different realizations, we chose to re-sample the whole population in each realization.

The KDE is initialized using the Λ_{ij} values as the weight for each system in order to maintain the distribution of galaxy properties that would be present in the universe. The properties we re-sample are total mass, mass ratio, redshift, frequency, g-r color, absolute magnitude, star metallicity, star formation rate, and stellar mass. The total mass, mass ratio, redshift, frequency, star formation rate and stellar mass are re-sampled in log space. Many of these properties have hard boundaries that are characteristic of that property. For example, mass ratio must be between 0 and 1. On the other hand some of the properties such as total mass should not be greater than $10^{11} M_{\odot}$, as this is not realistic in the simulation– Illustris does not produce any total masses this large. To solve both of these types of boundary requirements, we use reflective boundaries. Instead of cutting out systems that are drawn outside our boundary, they are reflected back inside the boundary. Systems that are drawn close to the boundary are better replaced with others close to the boundary rather than redrawn randomly. For the boundaries that were not inherent to the nature of the property but rather bounded by what is physically possible in Illustris, we reflected any systems that were outside the maximum and minimum of the original systems. Thus our distributions of properties are conservative as they don't extend beyond the limit in the simulation even though we produce more systems.

Using these draws of the systems, we calculated the characteristic strain for each binary and ultimately the GW spectra of each realization. Figure 2 shows the strain spectra for 5 of the 1000 realizations. To determine the systems for which to calculate the detection statistics, we considered only the loudest source in each frequency bin. For each of these loudest systems we calculate the DP.

The calculation of detection statistics is based on $\mathcal{F}_e$ statistics, which in the absence of signal is,

$$p_0(\mathcal{F}_e) = \mathcal{F}_e e^{-\mathcal{F}_e} \tag{2.6}$$

and with signal is

$$p_1(\mathcal{F}_e, \rho) = \frac{[2\mathcal{F}_e]^{1/2}}{\rho} I_1\left(\rho\sqrt{2\mathcal{F}_e}\right) e^{-\mathcal{F}_e - \frac{1}{2}\rho^2}. \tag{2.7}$$

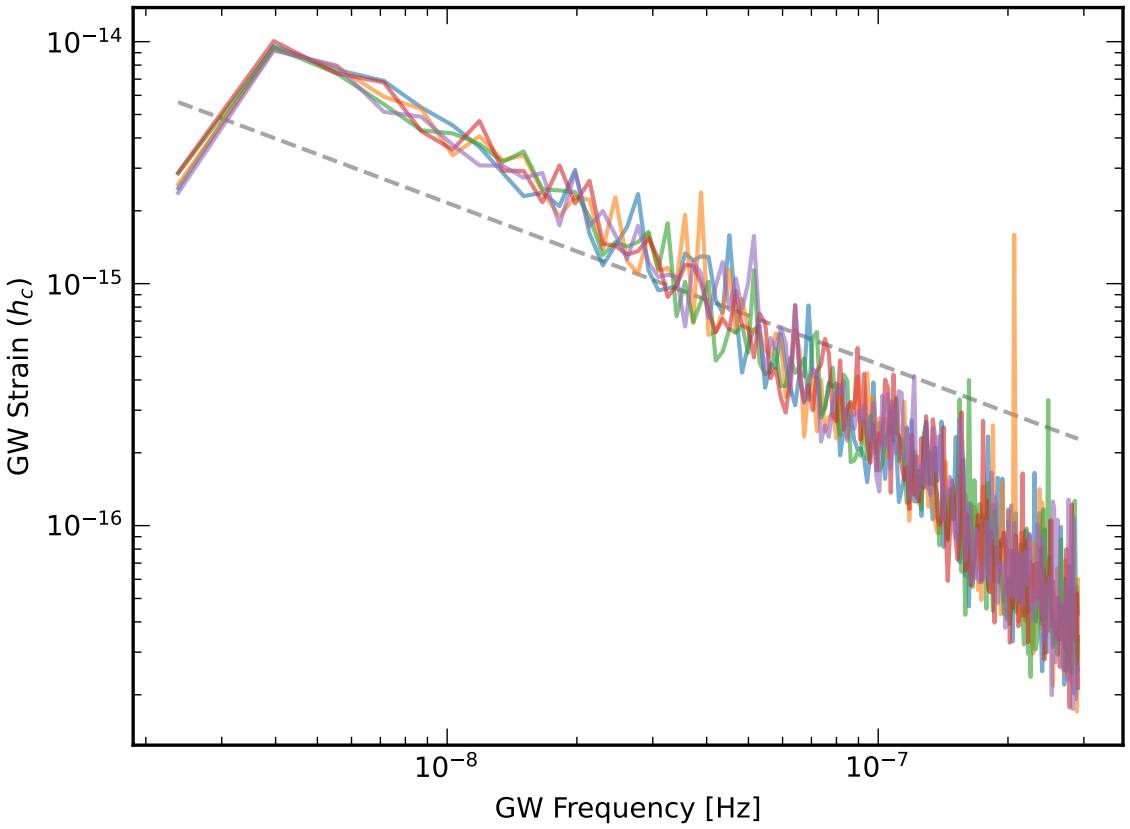

Figure 2: Each of the different colors is a different re-sampled realization. This plot contains 5, but there were 1000 total. The dashed gray line is the power law GWB spectrum assuming evolution solely by GW. The degree of power-law is -2/3.

The false alarm probability (FAP), α_0, is

$$\alpha_0 = 1 - [1 - [1 + \bar{\mathcal{F}}_e] e^{-\bar{\mathcal{F}}_e}]^N, \tag{2.8}$$

which is a function of N, the number of templates. We followed Rosado et al. (2015) and use $[N = 10^4]$ as the number of templates. From there, we can numerically integrate Equation 2.7 to get the detection probability (DP) of single source in its frequency bin,

$$\gamma_i = \int_{\bar{\mathcal{F}}_e}^{\infty} p_1(\mathcal{F}_e, \rho) d\mathcal{F}_e. \tag{2.9}$$

I_1 is a modified Bessel function of the first kind of order 1. It causes an overflow when the argument it large. The large argument expansion solves this issue. Using artificial SNR values we crafted an interpolant that spanned the whole range of detection probabilities and is a fast and safe way to convert from the calculated signal to noise ratio to the detection probability.

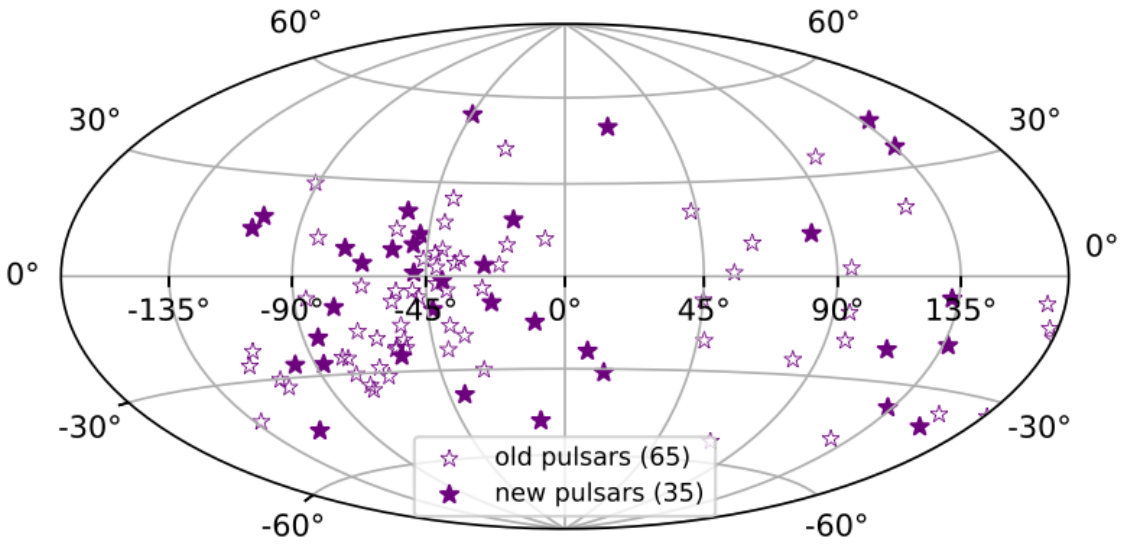

Figure 3: 65 old IPTA 2nd data release pulsars and 35 new re-sampled pulsars.

This equation requires that we know $[\rho = S/N_s]$. This is calculated as follows.

$$S/N_S = [\sum_{i=1}^{M} S/N_i^2]^{1/2}. \tag{2.10}$$

The squared signal of each individual pulsar $[S/Ni^2]$ can be calculated using Equation (*).

$$\begin{aligned} S/N_i^2 = \frac{A^2}{S_i 8\pi^3 f^3}[a^2[F_i^+]^2[\Phi_T[1+2\sin^2(\Phi_0)] \\ +\cos(\Phi_T)[-\sin(\Phi_T))+4\sin(\Phi_0)]-4\sin(\Phi_0)] \\ +b^2[F_i^x]^2[\Phi_T[1+2\cos^2(\Phi_0)]+\sin(\Phi_T)[\cos(\Phi_T)-4\cos(\Phi_0)]] \\ -2abF_i^+F_i^x[2\Phi_T\sin(\Phi_0)\cos(\Phi_0)+\sin(\Phi_T)[\sin(\Phi_T)-2\sin(\phi_0)] \\ +2\cos(\Phi_T)\cos(\Phi_0)-2\cos(\Phi_0)]] \end{aligned} \tag{2.11}$$

where F^+ and F^x are the GW antenna response patterns for each pulsar.

The pulsar array we create uses the 65 pulsar in the IPTA second data release (Perera et al., 2019) and then re-samples 35 more from the locations of the original 65 pulsars for a total of 100 pulsars–a reasonable array for what could be possible within this decade. Figure 3 shows the sky location of these new pulsars. Noise parameters are selected as realistic properties from scenario c in Kelley et al. (2018), which is $h_c^N(f = 0.1\text{yr})$ of 6.7 $\times 10^{-15}$, σ_{WN} as 0.3μs, A_{RN} as 1 $\times 10^{-15}$, γ_{RN} as -4.5,

$$S_{\rm RM} = \frac{A_{\rm RM}^2}{12\pi^2}\left(\frac{f}{f_{\rm ref}}\right)^{\gamma_{\rm RN}} f_{\rm ref}^{-3}. \tag{2.12}$$

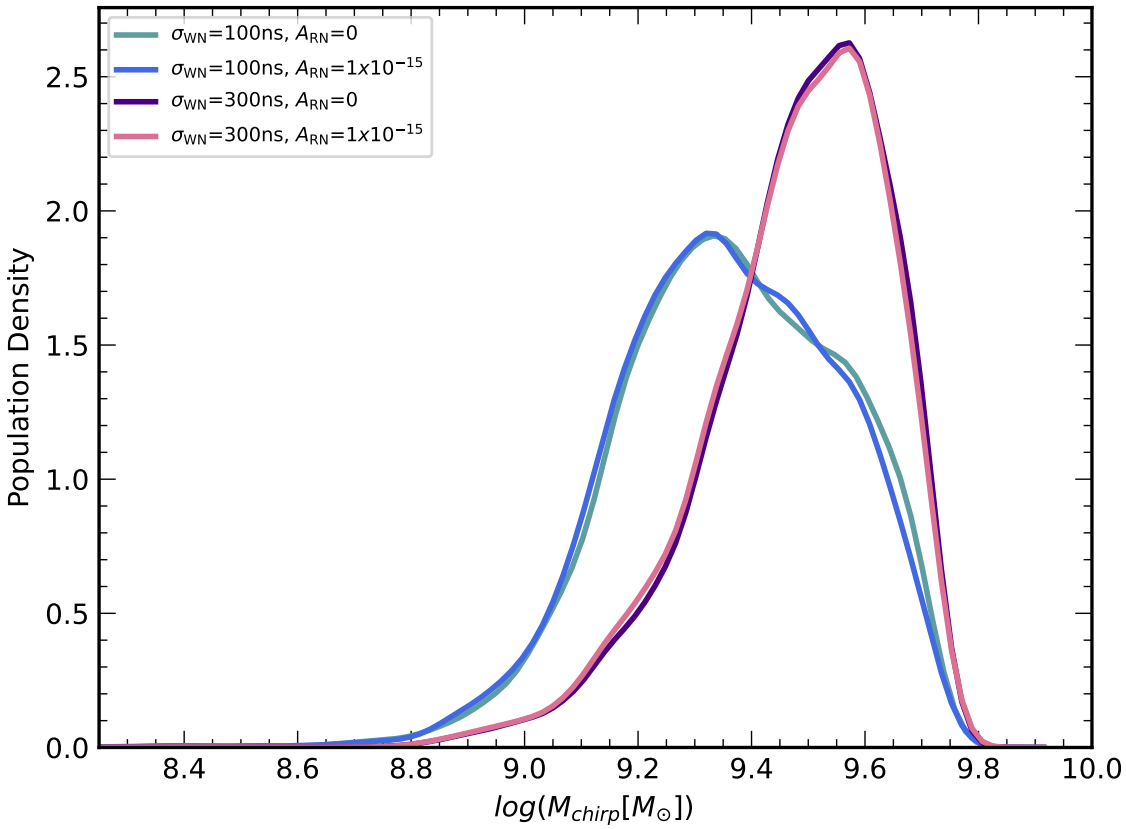

Figure 4: Each of the lines in this histogram are the detection probability weighted chirp mass distribution with different noise characteristics. The bottom option (pink in color) are the properties used in the rest of our plots. With larger noise properties the distributions are shifted towards higher chirp mass systems being the most detectable.

PTAs are highly heterogeneous in noise properties—some being much better than others. The white noise properties will also improve with time. Figure 4 is a comparison of multiple noise characteristic's effect on the weighted chirp mass distribution. We see that the white noise is the greater determiner of distribution, and thus DP, than the red noise is. These factors are found within the spectral noise density,

$$S_i = 2\Delta t \sigma_i^2 + S_{h,\text{rest}} + S_{\text{RN}}. \tag{2.13}$$

The other factors include Δt as 2 weeks and $S_{h,\text{rest}}$ is the red noise produced by the remainder of the sources in each frequency bin. When the largest source is removed from each bin, the strain of the remaining sources left in each frequency bin is summed to get the background strain. In each realizations we calculate the DPs 1000 times for the loudest in each bin, taking the average in order to be less dependent on the randomness of the locations of the pulsars in each realization.

CHAPTER 3

Results and Discussion

In each of the following figures, we plot the original population in order to compare with the detection probability weighted one. This "original" population is the base population without the DP weighting. It represents all the MBH that merge in Illustris (and their hosts) and make it through the various cuts and filters at the time-step when they produce GW in the PTA range. The population is weighted by its Λ_{ij} value (Equation 2.4) and re-sampled, thus representing the real population of this type of galaxies. This is not the whole population of all galaxies in the universe, but is rather the unweighted population. It is used merely for comparison and to indicate which properties are more starkly different in detectable galaxies than galaxies in a population closer to the overall population. We will not make many quantitative analyses of this original population, and it should be regarded as a visual aid.

For example, in Figure 5 the blue, original population, does not represent the distribution of the chirp mass of all galaxies. Chirp mass, by definition, means this plot only includes galaxies with a black hole binary and cannot be the total galaxy population. The population is cut off at $10^6 M_\odot$ because only above this threshold are they possibly detectable and accepted in the original cuts made of the Illustris systems (Sec. 2.1). Additionally, the redshift distribution does not include very large redshift systems as these systems would not be as old and thus less likely to have massive enough black holes to pass the cut for Illustris.

3.1 MBHB Population

Over 1000 realizations there are 140 systems that have a DP above 90%. An average of 0.14 systems per universe that we declare detectable by being predominant in the realizations by having such a high DP. Rosado et al. (2015) find that even 20 years from now the DPs for individual sources only reach 10%-20% with current IPTA at the time of the paper. However, they suggest that with the addition of more pulsars and slightly less constraining noise parameters and detection requirements there could be sources with 80% DP after 10 years. In this light our very small number of systems above 90% seem more reasonable. Additionally, our main concern in this thesis is to look at the host galaxy properties that would eventually be detected, not give the most robust prediction of when and how many will be predicted.

The DP weighted distributions of chirp mass and redshift align with expectation. The DP weighted chirp mass distribution, Figure 5, is in the highest mass range, in the high mass tail of the original population. The DP weighted redshift in Figure 6 is shifted towards smaller redshift, meaning closer systems that produce louder GW signals are the most detectable. These are expected results given Equation 1.2.

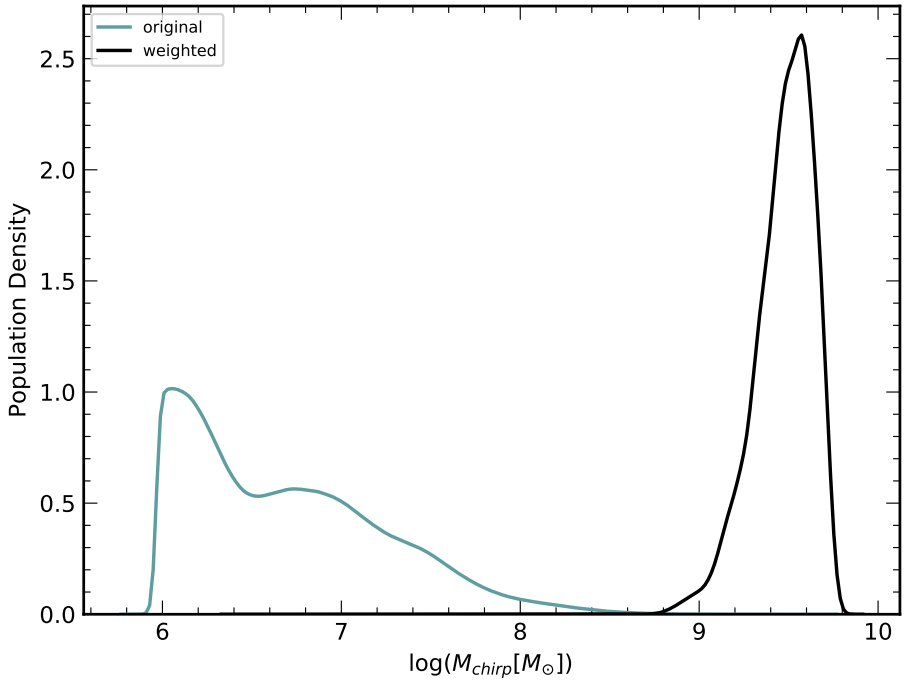

Figure 5: Distribution of the log of the chirp mass. The black distribution is the DP weighted distribution and is shifted towards higher chirp mass. The reflective boundary at the most massive is 1.33×10^{10}. Any larger value is reflected back across the boundary.

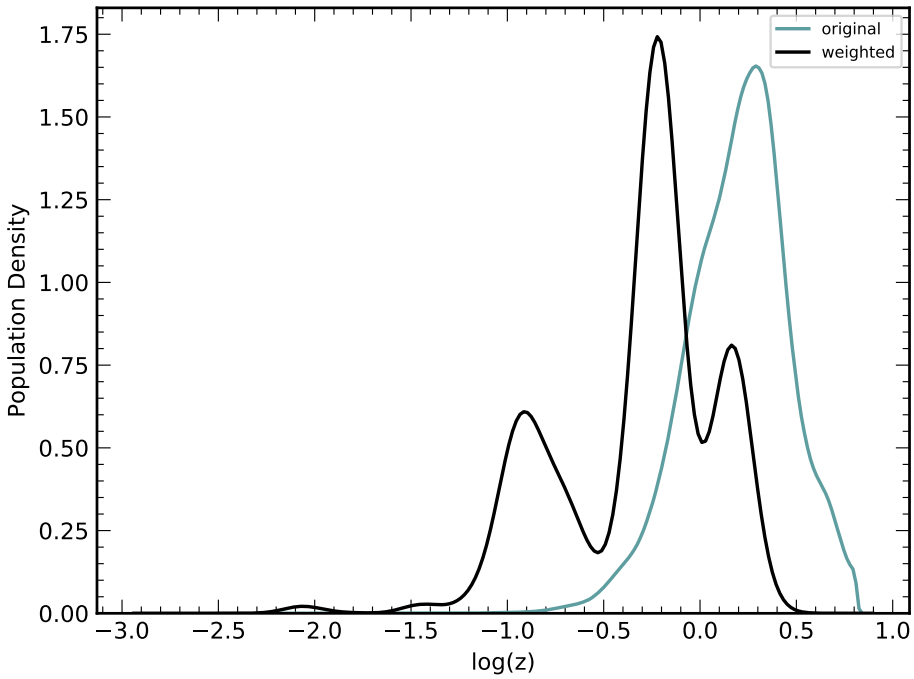

Figure 6: Distribution of the log of the redshift. The black distribution is the DP weighted distribution and is shifted towards lower and thus closer redshifts.

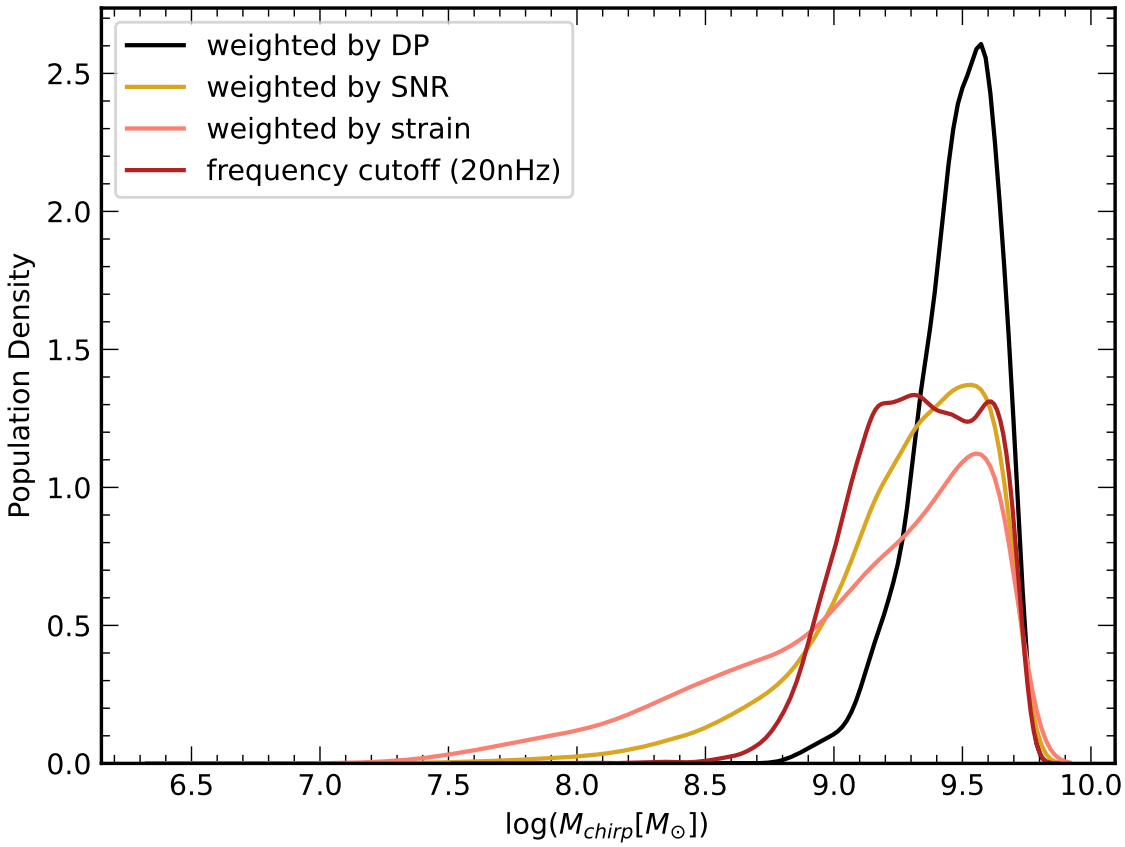

Figure 7: The distributions of the chirp mass with different weighting schemes. The yellow is weighted by the SNR (Equation 2.11) and peaks at approximately the same point at the DP weighted plot. The orange is weighted by the strain of the binary (Equation 1.2 and displays more weight at lower mass as strain is less dependent on chirp mass than DP. The red plot is using a frequency cutoff of below 20 nHz. It has a less formed peak but is localized in the same chirp masses as the DP weighted distribution.

3.2 Different Weightings

The DP is not the only metric that can be used to weight the distributions of properties. DP is perhaps the robust, but also is more computationally intensive. If there is another more simple method that achieves comparable results that would be useful. We compared weighting different distributions by the DP, SNR, strain, and frequency cutoff. In Figure 7, we see each of these metrics compared on the chirp mass distribution. Each of the distributions peak close to the same point. The SNR and strain weightings have longer tails in the lower mass area suggesting that neither is as dominated by the highest chirp mass. When only considering the systems with a frequency below 20 nHz, the distribution also closely resembles the DP weighted one. It is important to note that the frequency cutoff is applied only to the loudest sources in each bin, not the whole population. However, the fact that a frequency cutoff could be used to approximate a DP weighting is very useful as an approximation that requires much less computation. The distributions are similarly close with the other MBHB and host galaxy properties.

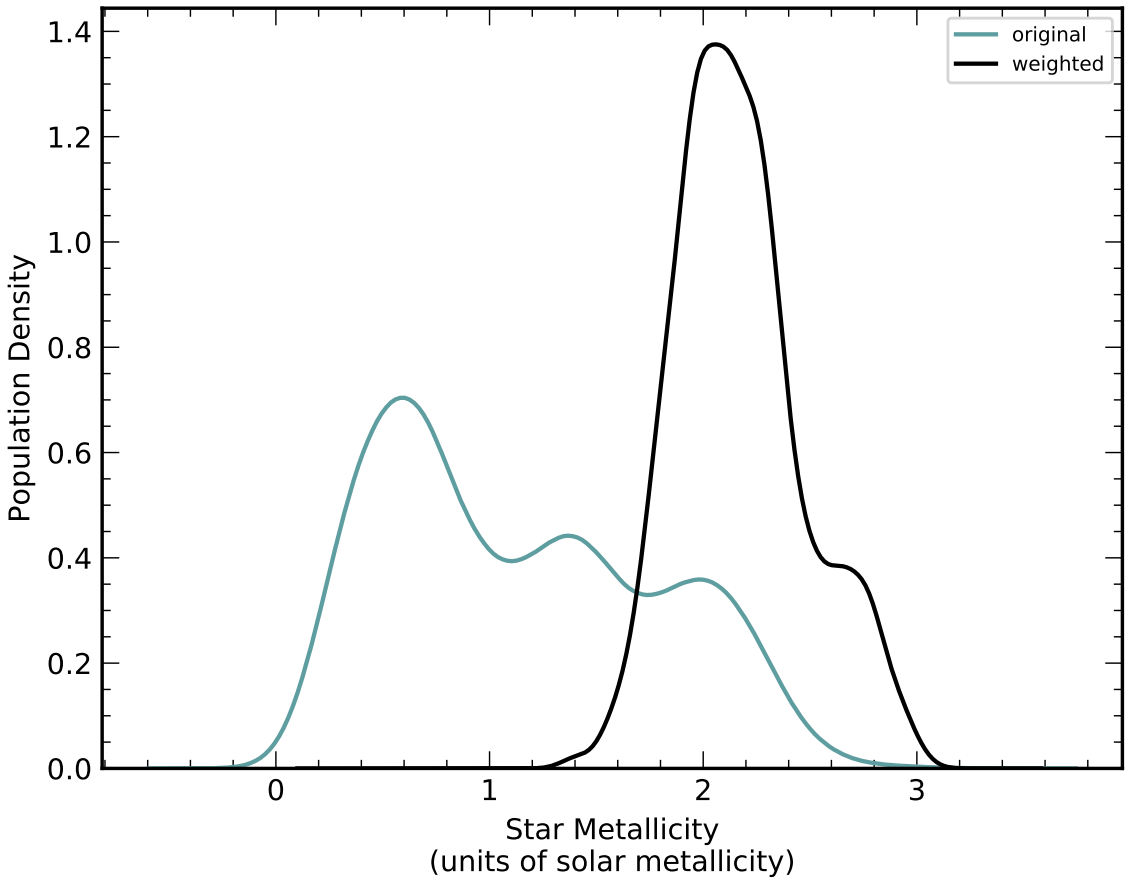

Figure 8: Distribution of the star metallicity. The black distribution is the DP weighted distribution and is shifted towards higher star metallicity, peaking around twice solar metallicity. The blue, original population peaks at around 0.6 solar metallicities. This is the property with one of the most stark differences between the original population and the DP weighted one.

3.3 Star Metallicity

The star metallicity is a mass-weighted average metallicity–the fraction of mass that is above Helium–of the star particles bound to the subhalo in Illustris. It is restricted to stars within twice the stellar half mass radius. We use this property as the star metallicity of the galaxy. Figure 8 shows that the most detectable systems are in galaxies where the star metallicity is around twice solar metallicity. This is in sharp contrast to the overall population which peaks nearer to 0.6 solar metallicities. In general, galaxies with a high solar metallicity are older. Star metallicity increases with each generation of stars because the heavier metals are formed in the cores of stars. In other words the older the galaxy, the more generations of stars, the higher the metallicity. Older galaxies have also gone through more mergers and are more likely to have a MBHB system large enough to be detectable. This property is one of the most starkly different than the original population and could be one of the best for ranking a galaxies likelihood of being a single source GW signal host specifically because it is an observable property (Wu, 2020).

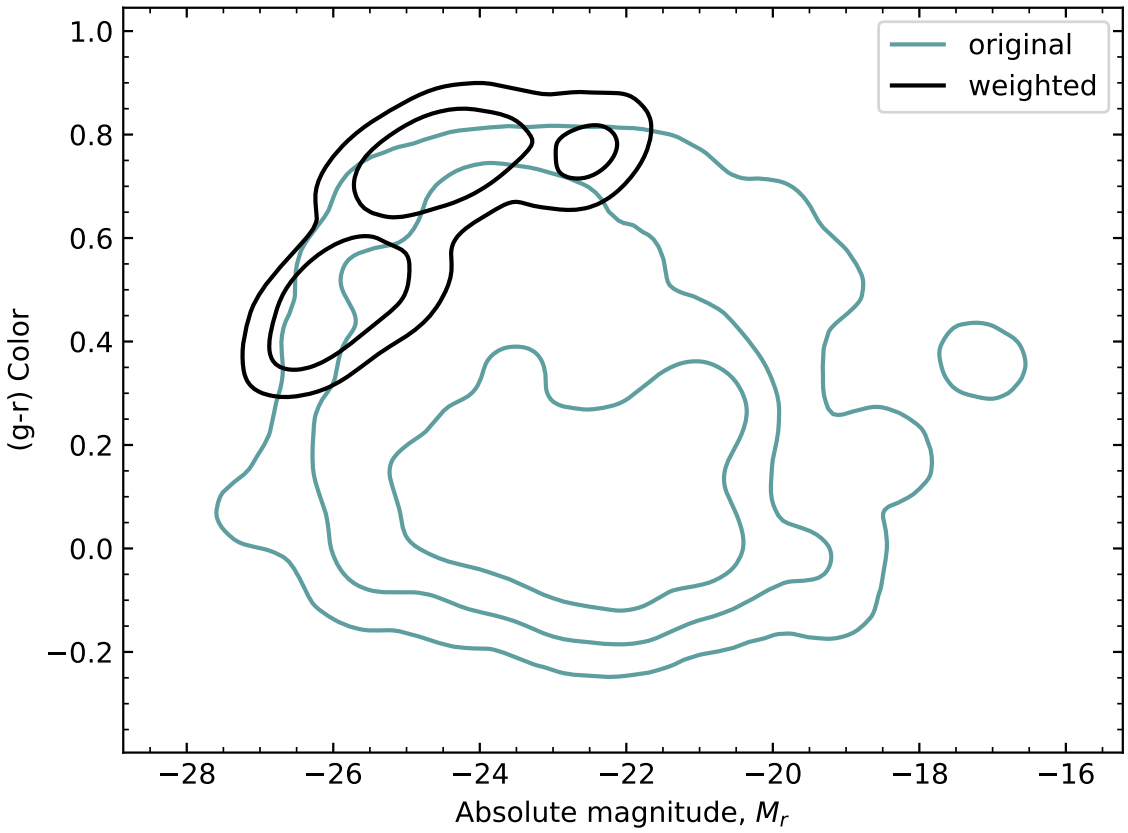

Figure 9: In the color-magnitude diagram, the blue lines, the original population, have contours at 68%, 95%, and 99.7%, or one, two, and three sigma. The black, weighted population has contours at one and two sigma only. The most detectable systems are high in g-r color and more negative in absolute magnitude than the original population.

3.4 Color Magnitude

Figure 9 shows the visual appearance of the most detectable host galaxies. G-R color is the subtraction of the g and r light bands that gives an indicator of the color of the stars in a galaxy. This is plotted against the absolute magnitude of the galaxies, the indicator of inherent brightness. We used the V band as the indicator of absolute magnitude. The most detectable galaxies have a higher g-r color indicating they more red in color. They have more negative absolute magnitudes meaning they are also brighter. Thus, brighter and more red galaxies are the most detectable.

Brighter and more red galaxies indicate that the most detectable galaxies are elliptical galaxies. We expect this result as galaxies become more elliptical after many mergers with other galaxies. The mergers causes what spiral structure may have existed in the galaxies to get disturbed. After enough mergers the galaxy no longer has any spiral structure and may be considered elliptical. Many mergers are expected in order to grow such a large galaxy that can contain a large enough black hole binary to produce PTA detectable GW. We now have a range of color and magnitude where these galaxies would be expected to fall.

3.5 All Properties

Figure 10 shows the two dimensional distributions of all the various properties with one another. We have previously discussed the color magnitude plot in detail and will not go into depth in all the comparisons, but each of the comparisons offers valuable information on the correlations between all the different parameters.

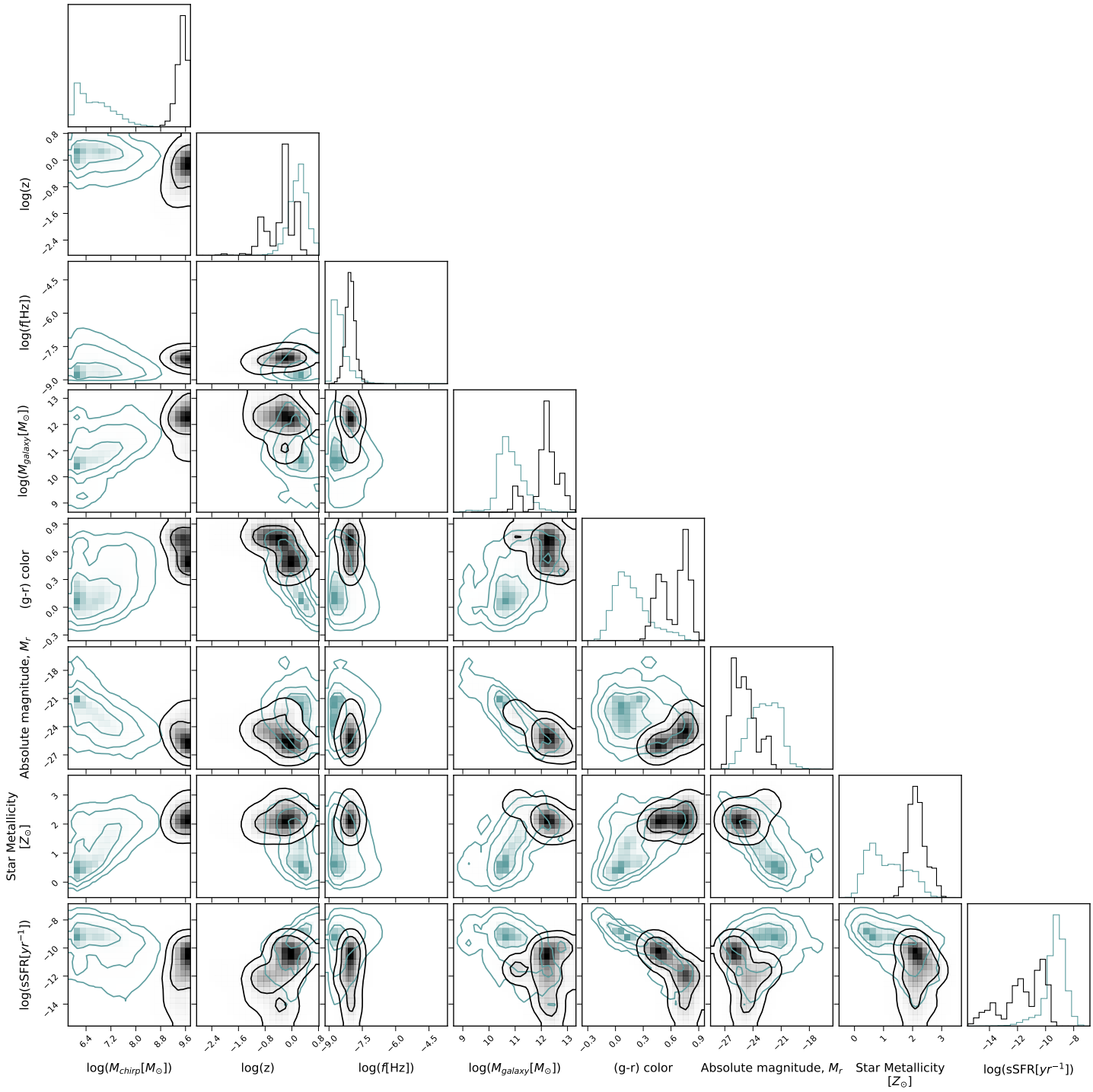

Figure 10: Two dimensional distributions comparing all the properties. The blue lines, the original population, have contours at 68%, 95%, and 99.7%, or one, two, and three sigma. The black, weighted population has contours at one and two sigma only.

CHAPTER 4

Conclusion

Individually resolvable single sources producing GW are expected to be detectable by PTA in the near future, most likely after the detection of the GW background. The sky-localization of PTA has very low resolution, and thus is unable to pinpoint the specific host galaxy of the MBHB system producing the detectable signal. It is thus useful to analyze the properties of the host galaxies of the most detectable MBHB.

We use the Illustris cosmological simulations coupled with semi-analytic post-processing to identify the host galaxies in Illustris at the time we calculate they are PTA detectable. Each of these properties is weighted by the detection probability (DP). We find that weighting by the signal to noise ratio or strain produce similar distributions, but even more similar is the distribution with simply a frequency cutoff at 20 nHz. The largest systems in their respective frequency bin with a frequency less than 20 nHz have a very similar distribution to the DP weighted distribution. This is useful as a computationally inexpensive estimate of the most detectable properties. Using the DP, we found that there was an average of 0.14 systems per universe realization that have a DP greater than 90%. Of the various host galaxy properties the star metallicity has the most contrast upon weighting by detectability. The original unweighted population peaks at $\sim$0.6 solar metallicities while the DP weighted distribution peaks at twice solar metallicity. The color magnitude diagram gives an indication of the visual appearance of the most detectable galaxies. They are more red and bright indicating they are most likely elliptical galaxies whose spiral structure has been destroyed my many galaxy mergers.

Each of the distribution of host galaxy properties gives us a tool to rank host galaxies by their likeliness of being the host of a detected single source, a very useful tool for multi-messenger astronomy. A natural next step for future work is to look at the properties of the MBHB that would produce detectable electromagnetic counterpart signatures. Side by side with the population that is detectable by PTA, investigated in this work, we can find the overlap in the two populations. This would give the properties of the MBHB that are most likely to have multi-messenger detection.

References

Abbott B. P., et al., 2016, Phys. Rev. Lett., 116, 241103

Anholm M., Ballmer S., Creighton J. D. E., Price L. R., Siemens X., 2009, Phys. Rev. D, 79, 084030

Antonini F., Merritt D., 2011, The Astrophysical Journal, 745, 83

Antonini F., Merritt D., 2012, , 745, 83

Blecha L., et al., 2016, , 456, 961

Burke-Spolaor S., et al., 2019, The Astronomy and Astrophysics Review, 27

DeGraf C., Sijacki D., Di Matteo T., Holley-Bockelmann K., Snyder G., Springel V., 2021, Monthly Notices of the Royal Astronomical Society, 503, 3629–3642

Genel S., et al., 2014, , 445, 175

Gould A., Rix H.-W., 2000, The Astrophysical Journal, 532, L29

Hellings R. W., Downs G. S., 1983, , 265, L39

Hobbs G., et al., 2010, Classical and Quantum Gravity, 27, 084013

Holley-Bockelmann K., Khan F. M., 2015, The Astrophysical Journal, 810, 139

Hulse R. A., Taylor J. H., 1975, , 195, L51

Katz M. L., Kelley L. Z., Dosopoulou F., Berry S., Blecha L., Larson S. L., 2020, , 491, 2301

Kelley L. Z., Blecha L., Hernquist L., 2017, , 464, 3131

Kelley L. Z., Blecha L., Hernquist L., Sesana A., Taylor S. R., 2018, Monthly Notices of the Royal Astronomical Society, 477, 964–976

Kramer M., Champion D. J., 2013, Classical and Quantum Gravity, 30, 224009

Magorrian J., Tremaine S., 1999, , 309, 447

Manchester R. N., et al., 2013, , 30, e017

McLaughlin M. A., 2013, Classical and Quantum Gravity, 30, 224008

McWilliams S. T., Ostriker J. P., Pretorius F., 2014, The Astrophysical Journal, 789, 156

Merritt D., 2013, Classical and Quantum Gravity, 30, 244005

Merritt D., Milosavljević M., 2005, Living Reviews in Relativity, 8

Perera B. B. P., et al., 2019, Monthly Notices of the Royal Astronomical Society, 490, 4666–4687

Peters P. C., 1964, Physical Review, 136, 1224

Rosado P. A., Sesana A., Gair J., 2015, Monthly Notices of the Royal Astronomical Society, 451, 2417–2433

Sesana A., Vecchio A., 2010, , 81, 104008

Vogelsberger M., et al., 2014a, , 444, 1518

Vogelsberger M., et al., 2014b, , 509, 177

Wu Y.-Z., 2020, The Astrophysical Journal Letters, 893, L33